Morphology-controllable synthesis of $LiCoPO_4$ and its influence on electrochemical performance for high-voltage lithium ion batteries

Xiaochao Wu [a, b, e, *], Maria Meledina [c, d], Hermann Tempel [a], Hans Kungl [a], Joachim Mayer [c, d], Rüdiger-A. Eichel [a, b]

a Forschungszentrum Jülich, Institute of Energy and Climate Research (IEK-9, Fundamental Electrochemistry), D-52425 Jülich, Germany

b RWTH Aachen University, Institute of Physical Chemistry, D-52074 Aachen, Germany

c RWTH Aachen University, Central Facility for Electron Microscopy, D-52074 Aachen, Germany

d Forschungszentrum Jülich, Ernst Ruska-Centre (ER-C) for Microscopy and Spectroscopy with Electrons, D-52425 Jülich, Germany

e Polymer Technology Group Eindhoven (PTG/e) B.V., P.O. Box 6284, 5600 HG Eindhoven, The Netherlands

* Corresponding author. E-mail address: xi.wu@fz-juelich.de, xiaochao.wu@ptgeindhoven.nl (X. Wu)

Abstract

$LiCoPO_4$ is a candidate cathode material for 5V lithium ion batteries, but in practice it often suffers from the poor electrochemical performance due to its intrinsically slow ionic diffusion. Herein, various $LiCoPO_4$ materials with different morphology, including unstructured nanoparticle, nanorod and microrod shape, have been synthesized by solvothermal methods and a subsequent annealing process in air. Electrochemical analysis shows that the controllable morphology has an influence in electronic and ionic pathways, thus affects the electrochemical performance. The nanorod shape $LiCoPO_4$ shows the largest discharge capacity, the best rate capability and best cycling stability. Furthermore, the apparent Li^+ ion diffusion coefficients of $LiCoPO_4$ samples were determined to investigate the influence of particle shape and the orientation on the Li^+ ions migration.

1. Introduction

Popularization of portable electronics and electric vehicles worldwide stimulated the development of energy storage devices, especially lithium ion batteries [1, 2]. Nowadays, concerns are being raised regarding the suitability of lithium ion batteries for large scale application, which require tremendously high energy densities and an excellent thermal stability [3]. The traditional cathode materials, including $LiCoO_2$, $LiMn_2O_4$ and $LiFePO_4$, can hardly reach the required energy density. Due to the ever-growing demand for higher energy density that can reach 800 Wh kg^{-1}, intensive research is underway to identify and develop the new cathode materials with high intercalation voltage over 4.5 V (vs. Li/Li^+) [4, 5]. Since the redox potentials of Ni and Co are relatively high, the high voltage of cathode material can be attained by employing the compounds that contain these elements [6].

$LiCoPO_4$ is one of the most promising candidates to gain high energy density due to its high theoretical capacity (167 mAh g^{-1}) and high operating voltage (4.7 V vs. Li/Li^+). It was firstly reported by Amine *et al*. in 2000 [7], and it has been investigated from many aspects during the last decade [8-11]. $LiCoPO_4$ has an olivine crystal structure with three kinds of space groups: *Pnma*, *Pn2₁a* and *Cmcm*. Among the three polymorphs, the *Pnma* phase has the best electrochemical activity [12]. As illustrated in **Figure 1**, the unit cell of $LiCoPO_4$ with space group *Pnma* consists of CoO_6 octahedra and PO_4 tetrahedra. The CoO_6 octahedra form layers in the *bc* plane, which are cross-lined by PO_4 tetrahedra, creating a three-dimensional network [9, 13]. Each CoO_6 octahedron shares the corner with four other CoO_6 octahedra, resulting in the difficult delocalization of the electrons and thus the poor electronic conductivity [14]. The strong P-O bonds and the three-dimensional network can guarantee the dynamic and thermal stability of $LiCoPO_4$ [15]. LiO_6 octahedra share the edges and form tunnels along the [010] direction, and Li^+ ion diffusion is only promoted along this direction since the activation energy is significantly lower along this pathway [9, 16]. To accelerate the kinetic of Li^+ ions, one effective way is to shorten the [010] diffusion path for Li^+ ions release and insertion. Controlling the morphology and crystallographic orientation is thus vital for the battery

performance as these parameters determine the preferred direction of the Li^+ ions diffusion channel [17, 18].

Solvothermal synthesis route is a heterogeneous chemical reaction, which is performed in a closed system above the boiling point of the solvent at the ambient pressure [19]. By adjusting the synthetic parameters such as precursor, surfactants and solvents, it can offer additional flexibility in controlling particle size and morphology of the products. Wu *et al*. found that the particle size of $LiCoPO_4$ could be effectively controlled by changing the water/ethylene glycol ratio in the solvothermal synthesis [20]. Moreover, Ludwig *et al*. synthesized a series of $LiCoPO_4$ platelets by one-step microwave-assisted solvothermal route, using a variety of binary solvent blends of water and different organic co-solvents. There was a strong influence of the co-solvents on the morphology of $LiCoPO_4$, resulting in the formation of variations between square, rhombic and hexagonal platelets [21]. Up to now, some literatures have reported the investigation of solvents, but only a few reports on the effects of surfactants and additives on the solvothermal synthesis of $LiCoPO_4$ are available.

In this work, various $LiCoPO_4$ materials were synthesized by solvothermal method and a subsequent annealing process. Polyvinylpyrrolidone (PVP) and cetrimonium bromide (CTAB) were chosen as the additives due to their different functionalities in solvothermal solutions. Different morphologies of $LiCoPO_4$, including unstructured nanoparticle, nanorod and microrod shape, can be obtained by employing additives during the solvothermal process. The $LiCoPO_4$ samples were applied as the cathode materials of high voltage lithium ion batteries, and the influence of additives on morphologies and particle sizes and the correlation with the electrochemical performance was investigated. In addition, the apparent Li^+ ion diffusion coefficients of various samples were determined by electrochemical analysis techniques.

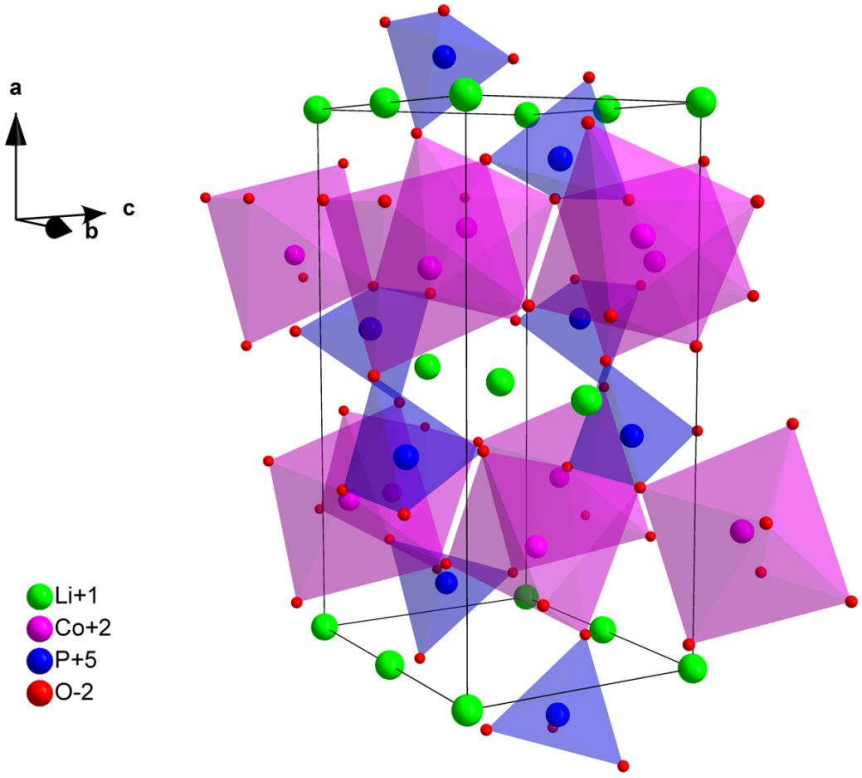

Figure 1. The schematic model of unit cell of $LiCoPO_4$ (*Pmna*).

2. Experimental section

2.1 Synthesis of bare $LiCoPO_4$ and $LiCoPO_4$ with different additives

Lithium hydroxide monohydrate ($LiOH{\cdot}H_2O$, 99.0%), diethylene glycol (DEG, $C_4H_{10}O_3$, 99.0%), polyvinylpyrrolidone (PVP, wt. 40000) and cetrimonium bromide (CTAB, $C_{19}H_{42}BrN$, 99%) were purchased from Sigma-Aldrich, cobalt(II) acetate tetrahydrate ($Co(CH_3COO)_2{\cdot}4H_2O$, 98.0~102.0%), ortho-phosphoric acid (H_3PO_4, 86%) and isopropanol (pure) were purchased from VWR chemicals. All chemical reagents were used as received. For the preparation of the precursor solution for the solvothermal reaction, 8 mmol $Co(CH_3COO)_2{\cdot}4H_2O$ and 8 mmol H_3PO_4 were firstly dissolved in a mixture of deionized water and DEG (1:1 vol/vol), which formed a homogenous red solution under continuous magnetically stirring. With

respect to the additives, 1 g of PVP or CTAB was then dissolved in the above prepared solution. The solution was bubbled with N_2 gas for half an hour to avoid the oxidation of the Co^{2+}. Afterwards, 24 mmol $LiOH \cdot H_2O$ were dissolved in the water/DEG mixture solution and then added to the above solution. The Co^{2+} and PO_4^{3-} concentration in the final precursor solution was 0.1 mol L^{-1}. The resulting mixture solution was transferred into a 125 mL Teflon-lined vessel for solvothermal reaction (Parr Instrument GmbH, Germany). The whole reaction process was kept at 180 ˚C for 24 hours, and afterwards the system was allowed to cool to room temperature freely. Then the obtained product was collected by centrifugation and washed with pure water and isopropanol, and dried in vacuum at 80 ˚C overnight. The final $LiCoPO_4$ powders without additive (named as LCP), $LiCoPO_4$ with PVP (named as LCP-PVP) powders and $LiCoPO_4$ with CTAB (named as LCP-CTAB) powders were obtained by annealing the precursor powders at 650 ˚C under air flow in a tube furnace for 5 hours.

2.2 Materials characterization

The crystallinity and phase analysis was carried out by powder X-ray diffraction (XRD) measurements between 10° and 80° in Bragg-Brentano-geometry with an EMPYREAN (Panalytical, Netherlands) X-ray diffractometer with Cu-K_α radiation operating at 40 kV, 40 mA. EXPGUI GSAS program was used for Rietveld refinement, and *Pnma* space group (ICSD_247497) for $LiCoPO_4$ was used as the basis data. Fourier transform infrared (FT-IR) spectra were collected in a wavenumber range of 400-1400 cm^{-1} with an ALPHA FT-IR spectrometer (Bruker, Germany). Elemental analysis was performed by inductively coupled plasma with optical emission spectroscopy (ICP-OES) for Li, Co and P contents, respectively. Approximately 10 mg of the powder samples were dissolved in a solution mixed by 3 mL HCl, 3 mL H_2O_2 and 3mL HNO_3, and then diluted to 50 mL volume. For the determination, two aliquots of the sample solution obtained were diluted and analyzed. Scanning electron microscopy (SEM) images were taken on a Quanta FEG 650 (FEI, USA) environmental scanning electron microscope operated at a voltage of 20 kV.

High angle annular dark field scanning transmission electron microscopy (HAADF-STEM) experiments were carried out using a FEI Titan G2 electron microscope operated at an accelerating voltage of 200 kV and equipped with a spherical aberration corrector unit. The samples were prepared by dispersing powder samples in ethanol and dropping the dispersion onto a carbon coated TEM copper grid.

2.3 Electrochemical measurements

The electrochemical performance was tested in Swagelok-type cells. The composite electrodes were prepared by mixing active materials, carbon black (Super P, Alfa-Aesar), and polyvinylidene fluoride binder (PVDF, Sigma-Aldrich) in a weight ratio of 7:2:1. The mixing process for the slurry was performed by an ARV-310 vacuum mixer (Thinky, Japan), and afterwards the slurry was tape casted onto the aluminum foil (thickness ~ 25 μm, Goodfellow, UK) by using semi-automatic film applicator ZAA 2300 (Zehntner, Switzerland). After the electrodes were dried under vacuum, an electric hot rolling press (MTI, USA) was used for the electrode densification. The assembly of the test half-cells was carried out in an argon filled glovebox, where the concentrations of water and oxygen were kept less than 0.1 ppm. Metallic lithium foil (Alfa-Aesar, Germany) was used as both counter and reference electrode. A glass fiber membrane (Whatman, UK) served as separator. As electrolyte 1 M $LiPF_6$ in a 1:1 solvent mixture of ethylenecarbonate (EC)/dimethylcarbonate (DMC) (LP30, BASF, USA) was used. Electrochemical tests were carried out at 25 ˚C in a climate chamber MKF120 (Binder, Germany). Galvanostatic charge/discharge tests, cyclic voltammetry (CV), and electrochemical impedance spectroscopy (EIS) measurements were conducted by a VMP3 potentiostat (Bio-Logic, France). The charge/discharge tests were performed at different current densities between 3.5 V and 5.0 V vs. Li/Li^+, and the C rate performance was measured by galvanostatic charging and discharging at C rates between 0.1C to 5C current (1C=166.6 mA g^{-1}). CVs were measured in a voltage window from 3.5 V to 5.2 V vs. Li/Li^+ at a scan rate from 0.05 mV s^{-1} to 0.5

mV s^{-1}. The EIS measurements were performed with 10 mV voltage amplitude in the frequency range from 200 kHz to 100 mHz for each half-cell.

3. Results and discussion

The structure and phase purity of bare $LiCoPO_4$ and $LiCoPO_4$ and with different additives were characterized by the X-ray diffraction (XRD), which is shown in **Figure 2**a. It can be seen that the main diffraction peaks of three samples illustrate the formation of orthorhombic $LiCoPO_4$ with a space group of *Pmna* that matches well with ICSD_247497. With respect to bare LCP without additive sample, trace amount of impurity phase was detected at around 22°, which was attributed to Li_3PO_4 (ICSD_77095, marked by '*'). The presence of Li_3PO_4 may be due to the incomplete reaction between raw materials [20]. On the other hand, no characteristic peaks of impurities were identified from LCP with different additives samples. Compared with the synthesis of bare LCP, the additives promoted the complete crystallization and resulted in the purity of $LiCoPO_4$ phase. To further investigate the lattice parameters and unit cell volumes of three samples, Rietveld refinement was performed based on the XRD data, and the results are presented in Figure S1 and Table S1. The lattice parameters and cell volumes of bare LCP and LCP with different additives are slightly different, and the influence of the additives on the structure will be discussed in the following section.

Attenuated total reflectance Fourier transform infrared (ATR FT-IR) spectra were carried out in the wavenumber range of 400-1200 cm^{-1} to study the vibrational spectrum of three samples, and the results are shown in **Figure** 2b. The absorption peaks located within the 400-700 cm^{-1} are due to the bending mode of the PO_4^{3-} polyanions, and the peaks in the range of 900-1200 cm^{-1} are caused by the stretching mode. The peaks at 460 cm^{-1} and 640 cm^{-1} belong to symmetric bending mode υ_2 and asymmetric bending mode υ_4 of PO_4^{3-}, respectively. Moreover, the peaks located at around 960 cm^{-1} are attributed to the symmetric stretching mode υ_1, while the three peaks located in the range of 1000-1150 cm^{-1} refer to the asymmetric

stretching mode υ_3 of PO_4^{3-}. In addition, the other observed peaks in the region of 500-590 cm^{-1} (marked by '#') are due to the asymmetric stretching modes of CoO_6 octahedra [22-25]. It was reported that the shift of υ_1 peak reflects the change of antisite defect concentration of phospho-olivine materials [11, 20]. In our system, there are no significant changes of the manifestation of functional groups on bare LCP and LCP with different additives reflected on the FT-IR spectra, indicating the similar levels on antisite defect concentrations of three samples. Based on the Rietveld refinements of XRD results (Table S2), the calculated antisite defect concentrations of bare LCP, LCP-PVP and LCP-CTAB samples are close, which is in agreement with FT-IR spectra. In addition, no absorbance peaks related to Li_3PO_4 in the FT-IR pattern of bare LCP without additive are found, probably due to the negligible amount of impurity [26].

ICP analysis was employed to measure the chemical composition of bare LCP and LCP with different additives, and the results are summarized in Table S2. It was found that the Co content in the material prepared without additive is lower compared with the other samples, which was due to the existing secondary phase of Li_3PO_4. When 4.97% secondary phase of Li_3PO_4 were subtracted (based on the Rietveld refinements results), the calculated molar ratio (marked as 'n*' in Table S2) became closer to the theoretical elemental ratio. With respect to LCP-PVP and LCP-CTAB, the values are closer to 1:1:1. Carbon contents were measured as well, and the contents are negligible, since the annealing atmosphere is air in order to avoid the formation of different carbon coating for the three samples.

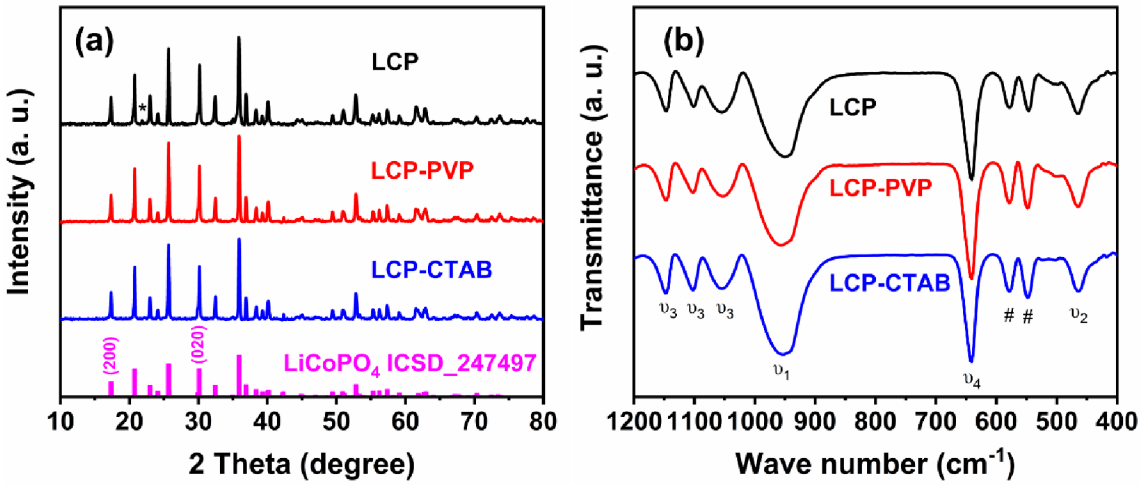

Figure 2. (a) XRD patterns and (b) FTIR spectra of bare $LiCoPO_4$ and $LiCoPO_4$ with different additives.

Morphological study of bare LCP and LCP with different additives samples were examined by scanning electron microscopy (SEM), as shown in **Figure 3**. There are recognizably different features between the samples prepared with and without additive. For LCP without additive sample (**Figure** 3a), it shows unstructured nanoparticle morphology with average size from 200 nm to 400 nm. On the whole, the LCP without additive particles distribute uniformly and no distinct agglomeration was observed in **Figure** 3b. With the additives, the morphological features changed dramatically. The presuming anisotropic adsorption of PVP and CTAB on the particle surface slowed down the crystal growth along [010] direction and resulted in such rod-like shape [27]. Besides, the employed DEG solvent with strong bonding effects on Co^{2+} on the {010} facets also helped in inhibiting the growth of $LiCoPO_4$ crystal along the [010] direction [28]. Furthermore, the precursor solutions' pH of LCP-PVP and LCP-CTAB is approximately neutral (around 7.5), which facilitated the maximum adsorption of H^+ on [100] and [010] direction and encouraged the anisotropic growth along the [001] direction which leads to the formation of rod shape morphology [29]. By calculating the intensity ratio between (020) and (200) XRD reflection peaks in Figure 2a, locating at 30.2° and 17.4°, the values of 1.97, 2.59 and 2.19 is obtained for bare LCP, LCP-PVP and LCP-CTAB sample, respectively. As compared with the standard data of 1.90 based on ICSD_247497, these samples show slightly increased $I_{(020)}/I_{(200)}$ values, which also indicates the preferred *ac*-plane orientation and the suppressed crystal growth along [010] direction [30]. However, the deviation of the intensity ratios from three samples are not that different, because the particles were not aligned in preferred orientation when conducting our XRD measurement [31]. Though they have the similar shapes, the particle sizes of LCP-PVP and LCP-CTAB are different. LCP-PVP particles possesses the diameter of about 200 nm and the length of about 1 μm (**Figure** 3d and 3e), while LCP-CTAB particles are roughly double the diameter as well as the length (**Figure** 3g and 3h). The effect may be due to the selective adsorption of different surfactant on $LiCoPO_4$ particle surface, which controlled the kinetic growth of various faces of crystals. In

addition, the polarities of nonionic PVP and ionic CTAB surfactant are different, which also played a role regarding to the different morphologies of $LiCoPO_4$ [32]. PVP is an amphiphilic nonionic surfactant, and it serves as a template during the solvothermal process. While CTAB is a cationic surfactant, it influences the charge density and lead to the formation of composite micelles in the solution [33]. The schematic representation of the morphological features of bare $LiCoPO_4$ and $LiCoPO_4$ with different additives is displayed in **Figure** 3c, f, i, which illustrates the three distinct morphologies of LCP obtained via different additives through solvothermal process. Additives with different chemical properties can affect the coordination of solvated species and the kinetics of the solvothermal reactions, thus resulting in the different specific morphologies of $LiCoPO_4$ products. Different morphologies of LCP particles are directly reflected in the specific area of the samples, which was characterized by N_2 adsorption/desorption measurements and shown in Figure S2 and Table S2. Bare LCP without additive has a BET area of 6.0 m^2 g^{-1}, which is comparable with our previous report for LCP annealed in N_2 [34]. LCP-PVP has the largest value of 9.5 m^2 g^{-1} mainly due to its small particle size. Because of the large diameter and length, LCP-CTAB has the lowest BET area of 2.9 m^2 g^{-1}, which is less than one third of LCP-PVP although they have the similar shapes.

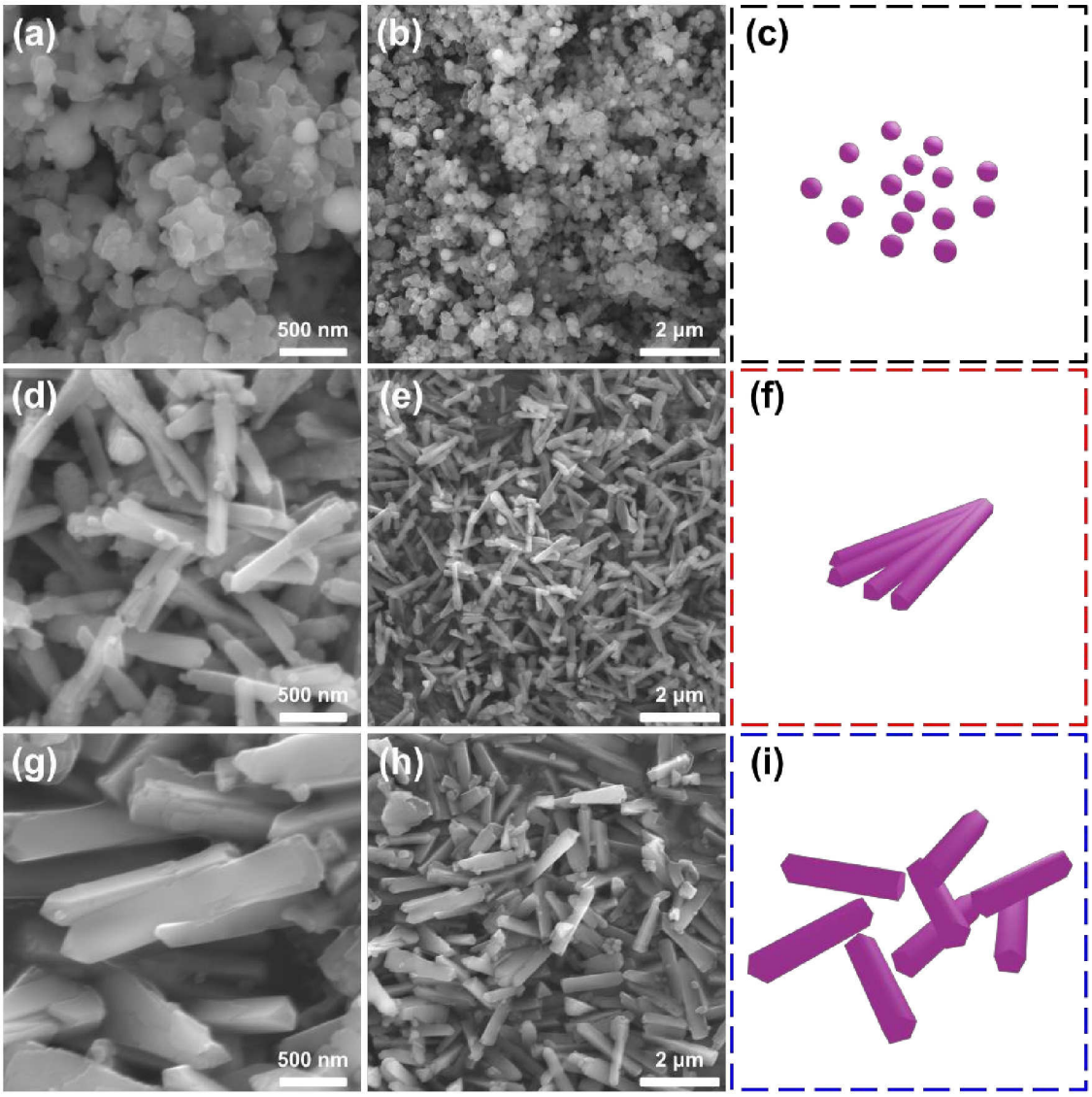

Figure 3. SEM images and the corresponding schematic models of bare $LiCoPO_4$ and $LiCoPO_4$ with different additives: (a, b, c) LCP without surfactant; (d, e, f) LCP-PVP; (g, h, i) LCP-CTAB.

HAADF-STEM imaging was exploited to investigate the morphology and crystal structure of the LCP-PVP sample. **Figure 4**a contains a HAADF-STEM overview showing a typical LCP-PVP particle with leek-like morphology: it is built of a "root" (Figure 4b) consisting of the nanoparticles with diameter of ~50 nm and several single crystal ~1-2 μm long and ~200 nm thick "stems" with sharp pronounced faceting (Figure 4c) growing out the "root". High resolution HAADF-STEM image of a "stem" crystal taken along the [010]

zone axis (imaged region is marked by an arrow in Figure 4c) together with a corresponding FFT is placed in Figure 4d. The "stems" tend to grow along the [001] direction and the "tunnels" in [010] directions, which provide the transport pathways for Li ions in the material, are perpendicular to the axis and ensure short distances and thus fast transport of Li to the center of the LCP-PVP stems. Moreover, the STEM analysis of LCP-CTAB sample was also conducted, shown in Figure S3. The overview image is similar with that of LCP-PVP, but with larger particle size, which is in agreement with SEM results. The "stem" LCP-CTAB crystal also grows along the [001] direction, indicating the same shape with LCP-PVP.

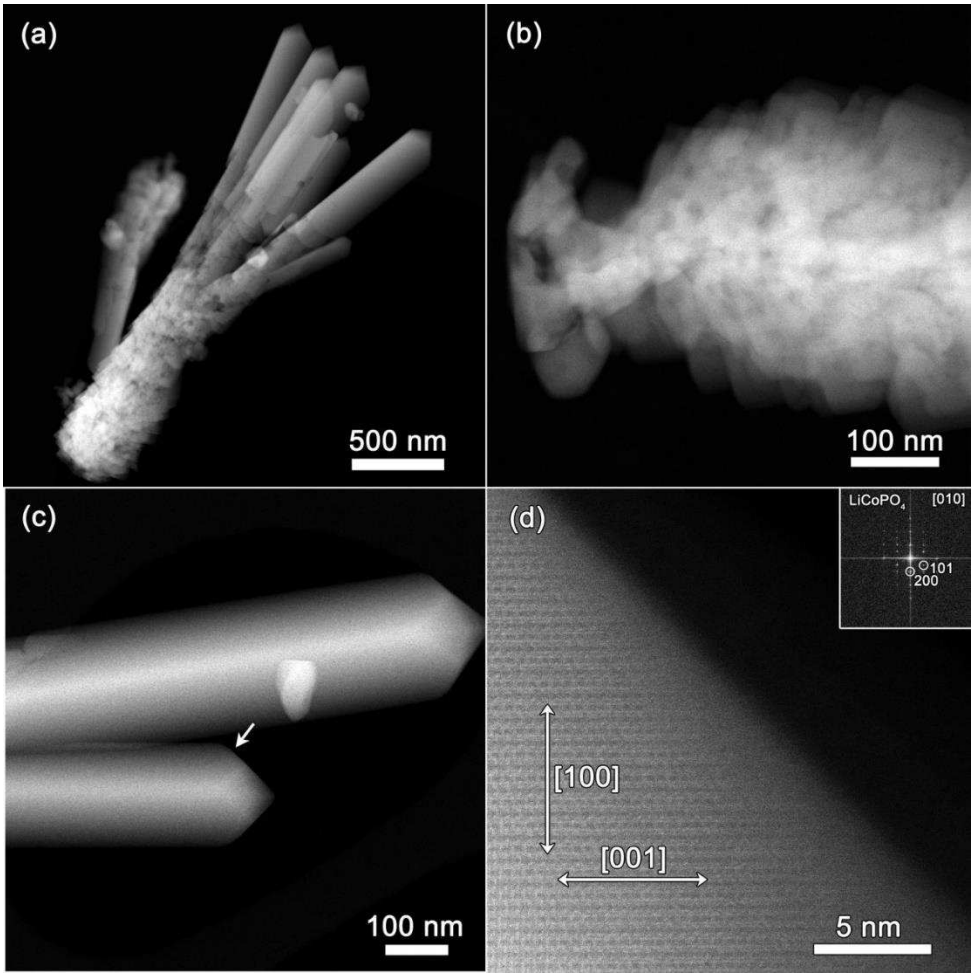

Figure 4. HAADF-STEM images of LCP-PVP material: (a) overview illustrating a typical leek-like morphology with (b) a "root", built of nanoparticles ~50-100 nm in diameter and (c) several single crystal "stems" of ~1-2 μm length. (d) HR HAADF-STEM image of LCP-PVP material taken along the [010] zone axis (from the "stem" region market by an arrow in (c) together with a corresponding FFT in the inset. The "stem" LCP-PVP crystal grows along the [001] direction.

In order to investigate the influence of sample morphology on electrochemical performance, galvanostatic charge/discharge tests between 3.5 V and 5.0 V (vs. Li/Li^+) were applied. The initial charge/discharge plots at 0.1 C based on LCP without and with different additives samples are displayed in **Figure 5**a. From all plots, two separated plateaus on both charge and discharge processes can be observed above 4.6 V. The first plateau of charge process occurred at around 4.80 V, involved the extraction of one third of Li^+ ions, while the second plateau was associated with the full delithiation of the active material, theoretically leading to delithiated $CoPO_4$. Due to the low current density, the delithiation/lithiation of $LiCoPO_4$ was comparatively complete. It displayed two separated plateaus in the discharge curves as well, indicating that the lithiation process from $CoPO_4$ to $LiCoPO_4$ also proceeds in two steps [34-37]. The bare LCP shows the first discharge specific capacity of 90.0 mAh g^{-1}, which is a comparable value for $LiCoPO_4$ without carbon coating [24, 34, 38]. LCP-PVP, with a capacity of 112.6 mAh g^{-1}, has the highest value among these three half-cells, while LCP-CTAB delivers the lowest discharge specific capacity of 70.8 mAh g^{-1}. On account of the fact that Li^+ ions only diffuse along the [010] direction, it is beneficial to have a short length on *b*-axis for materials to obtain good electrochemical performance. The higher discharge capacity of LCP-PVP is presumably due to its particle size and crystallographic orientation. Since LCP-PVP has a small average size along [010] direction, it also possesses a short Li^+ ion diffusion length. Besides, the nature of nanorods also promotes fast charge transport which aids LCP-PVP obtain high capacity [39]. Although LCP-CTAB has the rod-like shape, its shortest dimension of the single particle is still larger than those of other two samples, leading to the longest ionic diffusion pathway and lowest initial discharge capacity.

The long-term cycling performance at the current rate of 0.1 C is presented in **Figure** 5b. Obvious capacity fading can be found in all half-cells, especially in the first 5 cycles. Since a very limited amount of carbon coating was used to prevent the direct contact of active $LiCoPO_4$ with electrolyte, irreversible reactions could easily occur at high voltage, which mainly contributed to the degradation of active materials and capacity fading [40]. With respect to bare LCP, it can hardly keep reasonable capacity after 50 cycles. LCP-PVP retained the highest specific capacity of 70.5 mAh g^{-1} after cycling, which was 62% of the initial level.

LCP-CTAB also stayed more than half of the first discharge capacity, and it delivered higher capacity than bare LCP after cycling, though it had lower initial discharge capacity, indicating the rod-like shape morphology is beneficial to improve cycling stability of $LiCoPO_4$. SEM images of cathodes (including active materials, carbon black and binder) after cycling are shown in Figure S4. The rod shape of LCP-PVP and LCP-CTAB is stable for the $LiCoPO_4$ during cycling, however the surface morphology is subject to changes. The bare LCP shows a bigger size than its pristine sample, mainly due to the aggregation during cycling. Presumably the unstructured bare LCP particles cannot stay in their original state due to the volume change during cycling, and the aggregation gradually occurred during charging and discharging and resulted in the larger particle size and the capacity fading. Besides, there is no carbon coating on LCP particle surface, accelerating the side reactions with electrolyte at high voltage, which lead to the capacity fading additionally [41].

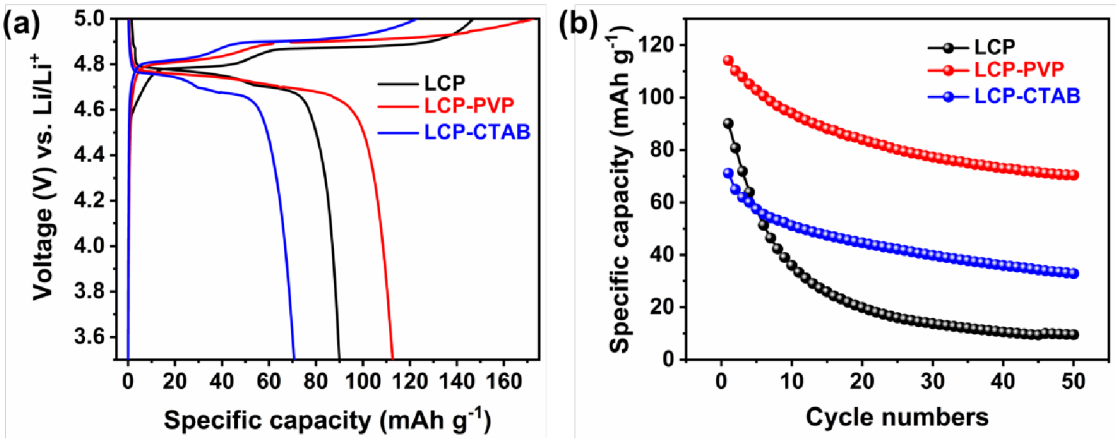

Figure 5. Electrochemical performance of bare $LiCoPO_4$ and $LiCoPO_4$ with different additives: (a) the initial galvanostatic charge/discharge plots at 0.1 C; (b) cycling stability at the current density of 0.1 C

Furthermore, the rate capability of bare LCP and LCP with different additives was tested with the same charge current rate of 0.1 C, and the initial discharge plots at various current rates are displayed in **Figure** 6a to 6c. With the gradual increase of current density, the discharge capacity goes down and the voltage

plateau becomes shorter induced by the restricted Li^+ ion diffusion. The high current rate capability shows a strong dependency on the morphologies of samples. LCP-PVP exhibits the best performance among the three half-cells, since it has the shortest Li ions diffusion length along [010] direction. The well-defined morphology can shorten the Li^+ ion diffusion length and improve the ionic conductivity, also decrease the charge transfer resistance of the electrode. On the other hand, bare LCP and LCP-CTAB display almost no electrochemical responses at 5C, which is probably because of the larger particles leading to the poor charge transfer kinetics of the bulk materials.

The results indicate that there is a strong influence of particle size and the orientation of the *b*-axis on the electrochemical reaction kinetics. LCP-PVP has nanorod shape with a diameter of around 200 nm, the shortest time for Li^+ ion diffusion during delithiation/lithiation process, as a result, it has the fastest Li^+ ion diffusion. Furthermore, the size of bare LCP without additive and LCP-CTAB reach to sub-micrometer or micrometer level, especially the length of *b*-axis. The distance to diffusion is relatively longer, which results in the slower Li^+ ion diffusion to the particle cores of bare LCP without additive and LCP-CTAB. In addition, although the capacity of LCP is lower than commercial $LiFePO_4$, it possesses high energy density when operating voltage is taken into consideration. The cell with LCP-PVP cathode delivers around 550 Wh kg^{-1} at 0.1 C, while many reported $LiFePO_4$ cathode have an energy density less than 500 Wh kg^{-1} due to the low discharge voltage (3.4 V vs. Li/Li^+). On the other hand, the strategies to improve the Li^+ ion transport properties by appropriate shapes and morphologies have been previously applied for $LiFePO_4$ [42, 43]. Our work also proves that rod-like shape is useful for a favorable electrochemical performance.

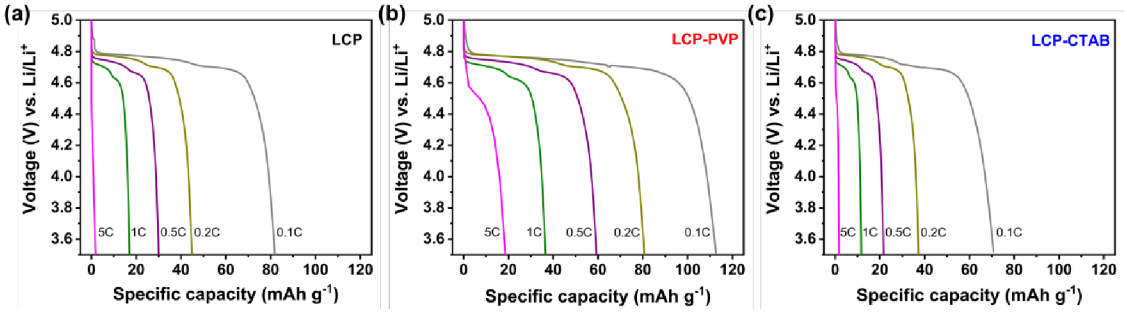

Figure 6. C-rate performance at various current rates from 0.1C to 5C of (a) bare LCP; (b) LCP-PVP and (c) LCP-CTAB.

The apparent Li^+ ion diffusion coefficients of bare LCP and LCP with different additives were determined using electrochemical impedance spectroscopy (EIS) as well as cyclic voltammetry (CV) on three half-cells. EIS was performed for them to determine the interfacial reaction resistance and the apparent Li^+ ion diffusion coefficients, as shown in **Figure** 7a. The spectra were fitted by using the equivalent circuit model (inset of **Figure** 7a), including ohmic resistances (R_s), charge-transfer resistance (R_{ct}), constant phase elements (CPE) and the Warburg impedance (Z_W). LCP-PVP shows the smallest charge-transfer resistance in high-middle frequency region, while LCP-CTAB has the largest one. In the low frequency region, the spectra reflect the Warburg impedance associated with the diffusion of Li^+ ion in the bulk electrode. Based on the sloping line in this region, the apparent Li^+ ion diffusion coefficients can be calculated by the following equation (Equation 1) [24, 40]:

$$D_{Li} = \frac{R^2T^2}{2A^2n^4F^4C^2{\sigma_w}^2} \qquad \textbf{(Equation 1)}$$

where R is the gas constant, T is temperature, F is Faraday's constant, σ_w (Warburg factor) is the slope of the linear fittings between real impedance and reciprocal square root of the angular frequency at low frequency region as shown in **Figure** 7b. The results of Warburg factor and Li^+ ion diffusion coefficient are presented in Table S3 as well. The values obtained from EIS vary from 1.67×10^{-14} cm^2 s^{-1} for LCP-CATAB to 4.69×10^{-14} cm^2 s^{-1} for LCP-PVP.

Figure 7c shows the CV curves at the scan rate of 0.05 mV s^{-1} for four half-cells. The peak locations are in agreement with the plateaus in **Figure** 5a. Specially, two oxidation peaks and only one broad reduction peak, which is due to the overlap of two indivisible peaks, can be observed in each CV curve. The intensities of reduction peaks are in consistence with the initial specific discharge capacity of bare LCP and LCP with different additives, and the unequal intensities of oxidation peaks and reduction peaks indicate the

irreversible side reactions. In addition, CVs at various scan rates from 0.05 mV s^{-1} to 0.25 mV s^{-1} were measured for each sample to determine the Li^+ ion diffusion coefficient, and the results are shown in Figure S5. As the scan rate increases, the cathodic and anodic peaks move to lower and higher voltages, respectively, with the increase of the peak current. The potential gap between redox couples became larger, indicating the larger electrode polarization. The cathodic and anodic current peaks were determined at each scan rate, and they were fitting as a line based on the square root of the scan rates (**Figure** 7d). The apparent Li^+ ion diffusion coefficients can be calculated according to the Randles-Sevick equation (Equation 2) [44, 45]:

$$\boldsymbol{I_p = 2.69 \times 10^5 n^{3/2} A D_{Li}{}^{3/2} C v^{1/2}} \qquad \textbf{(Equation 2)}$$

where I_p is the peak current, n is the number of electrons per molecule, A is the surface area of the electrode, D_{Li} is the Li^+ ion diffusion coefficient, C is the Li^+ ion concentration which can be calculated from the density and the molecular weight of the materials [46], and v is the scan rate. Based on the slope of the fitting line in **Figure** 7d, the apparent Li^+ ion diffusion coefficient of bare LCP and LCP with different additives can be calculated (Table S3). As can be expected, LCP-PVP exhibits the highest value of 4.20×10^{-14} cm^2 s^{-1} based on the cathodic current peaks, which is almost three times larger than for LCP-CTAB. The apparent Li^+ ion diffusion coefficient of bare LCP is not as high as for LCP-PVP, but higher than for LCP-CTAB. The diffusion coefficients determined from CV analysis show the same trend and similar values of those based on EIS analysis.

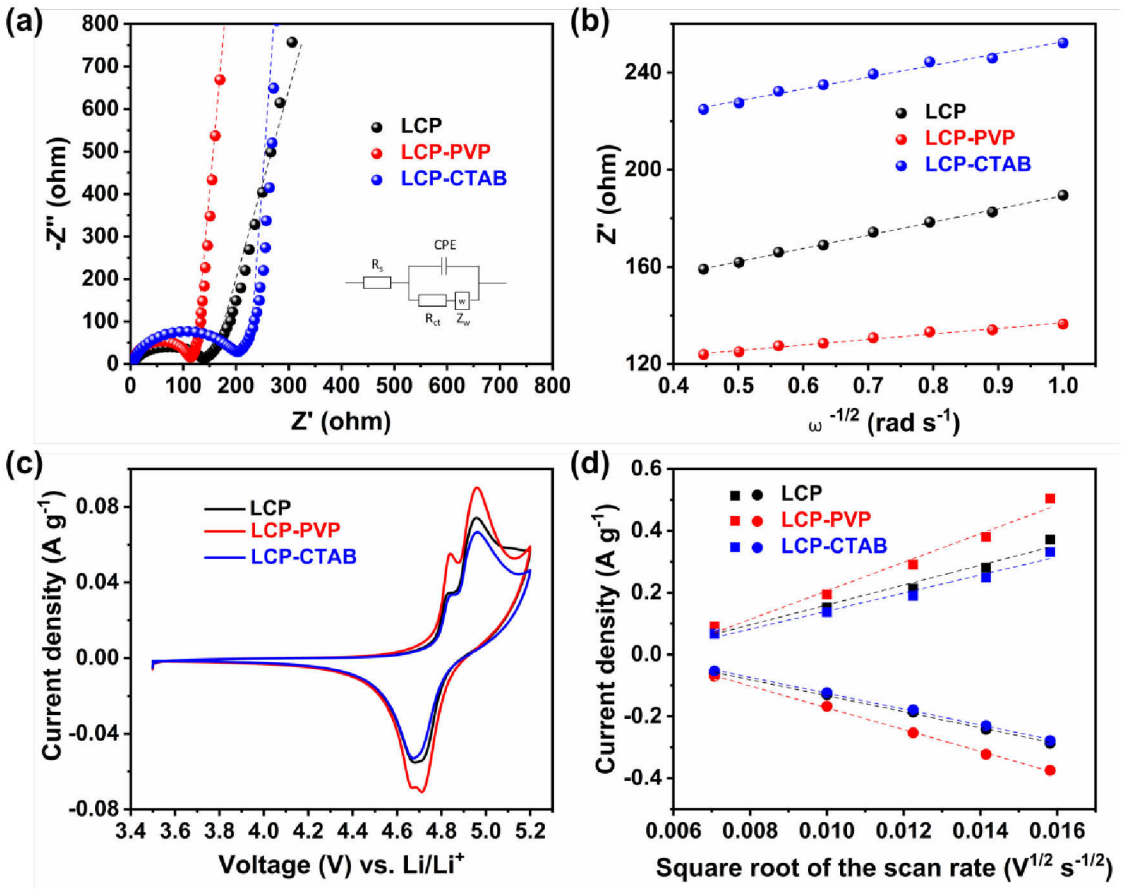

Figure 7. (a) Nyquist plots for the electrochemical impedance spectra and the equivalent circuit established for simulation; (b) linear fittings between real impedance and reciprocal square root of the angular frequency; (c) Cyclic voltammograms at a scan rate of 0.05 mV s^{-1}; (d) linear fitting of peak current and the square root of the scan rate.

4. Conclusion

$LiCoPO_4$ materials have been synthesized by solvothermal methods and a subsequent annealing process. SEM images exhibit that different morphology of $LiCoPO_4$, including unstructured nanoparticle, nanorod and microrod shape, can be obtained by employing different additives during the solvothermal process. HAADF-STEM analysis of orientations in the LCP-PVP revealed that the [010] direction are perpendicular to the rod axis, thus favoring short diffusion pathways to the inner parts of the material. The controllable morphology has an influence in electronic and ionic pathways, thus affects the electrochemical performance.

Electrochemical measurements demonstrate that LCP-PVP with the nanorod shape has the largest discharge capacity of 112.6 mAh g^{-1}, the best rate capability and best cycling stability. In addition, two electrochemical analysis techniques, based on EIS and CVs, were employed to determine the apparent Li^+ ion diffusion coefficients of bare LCP and LCP with different additives. The results indicate that there is a strong influence of sample morphologies and the orientation of *b*-axis on the Li^+ ion diffusion coefficient. The shape of $LiCoPO_4$ particle plays a critical role to influence the electrochemical reaction kinetics, and the morphology-controllable synthesis is an effective method to improve the electrochemical performance of $LiCoPO_4$ as the cathode material of high voltage lithium ion batteries.

Acknowledgments

The author X. Wu gratefully acknowledges a fellowship support by the China Scholarship Council (CSC) (No. 201506880008). Support by the German Ministry of Research and Education BMBF in the framework of the project MEET HiEND II is gratefully acknowledged. Furthermore, the support within the project 'SABLE' (03EK3543) by which the Quanta 650 FEI scanning electron microscope was provided is acknowledged.

References

[1] M. Li, J. Lu, Z. Chen, K. Amine, Adv. Mater., (2018) 1800561.

[2] X. Wu, Z. Lu, W. Zhu, Q. Yang, G. Zhang, J. Liu, X. Sun, Nano Energy, 10 (2014) 229-234.

[3] J. Liu, Adv. Funct. Mater., 23 (2013) 924-928.

[4] W. Li, B. Song, A. Manthiram, Chem. Soc. Rev., 46 (2017) 3006-3059.

[5] A. Kraytsberg, Y. Ein-Eli, Adv. Energy Mater., 2 (2012) 922-939.

[6] A. Mauger, C.M. Julien, M. Armand, J.B. Goodenough, K. Zaghib, Curr. Opin. Electrochem., 6 (2017) 63-69.

[7] K. Amine, H. Yasuda, M. Yamachi, Electrochem. Solid-State Lett., 3 (2000) 178-179.

[8] M. Zhang, N. Garcia-Araez, A.L. Hector, J. Mater. Chem. A, 6 (2018) 14483-14517.

[9] J. Ludwig, T. Nilges, J. Power Sources, 382 (2018) 101-115.

[10] S. Brutti, S. Panero, ACS Sym Ser, 1140 (2013) 67-99.

[11] X. Wu, M. Meledina, J. Barthel, Z. Liu, H. Tempel, H. Kungl, J. Mayer, R.-A. Eichel, Energy Storage Mater., 22 (2019) 138-146.

[12] K.J. Kreder, G. Assat, A. Manthiram, Chem. Mater., 27 (2015) 5543-5549.

[13] Y.H. Ikuhara, X. Gao, C.A.J. Fisher, A. Kuwabara, H. Moriwake, K. Kohama, H. Iba, Y. Ikuhara, J. Mater. Chem. A, 5 (2017) 9329-9338.

[14] A. Boulineau, T. Gutel, Chem. Mater., 27 (2015) 802-807.

[15] N. Membreño, K. Park, J.B. Goodenough, K.J. Stevenson, Chem. Mater., 27 (2015) 3332-3340.

[16] C.A.J. Fisher, V.M.H. Prieto, M.S. Islam, Chem. Mater., 20 (2008) 5907-5915.

[17] D. Morgan, A. Van der Ven, G. Ceder, Electrochem. Solid-State Lett., 7 (2004) A30-A32.

[18] N.H. Kwon, H. Yin, T. Vavrova, J.H.W. Lim, U. Steiner, B. Grobéty, K.M. Fromm, J. Power Sources, 342 (2017) 231-240.

[19] R.I. Walton, Chem. Soc. Rev., 31 (2002) 230-238.

[20] B. Wu, H. Xu, D. Mu, L. Shi, B. Jiang, L. Gai, L. Wang, Q. Liu, L. Ben, F. Wu, J. Power Sources, 304 (2016) 181-188.

[21] J. Ludwig, C. Marino, D. Haering, C. Stinner, H.A. Gasteiger, T. Nilges, J. Power Sources, 342 (2017) 214-223.

[22] Gangulibabu, D. Bhuvaneswari, N. Kalaiselvi, N. Jayaprakash, P. Periasamy, J. Sol-Gel Sci. Technol., 49 (2008) 137-144.

[23] M.T. Paques-Ledent, P. Tarte, Spectrochimica Acta Part A: Molecular Spectroscopy, 30 (1974) 673-689.

[24] K.J. Kreder, G. Assat, A. Manthiram, Chem. Mater., 28 (2016) 1847-1853.

[25] A. Rajalakshmi, V.D. Nithya, K. Karthikeyan, C. Sanjeeviraja, Y.S. Lee, R. Kalai Selvan, J. Sol-Gel Sci. Technol., 65 (2013) 399-410.

[26] X. Bian, Q. Fu, X. Bie, P. Yang, H. Qiu, Q. Pang, G. Chen, F. Du, Y. Wei, Electrochim. Acta, 174 (2015) 875-884.

[27] C. Neef, H.-P. Meyer, R. Klingeler, Solid State Sci., 48 (2015) 270-277.

[28] L. Peng, X. Zhang, Z. Fang, Y. Zhu, Y. Xie, J.J. Cha, G. Yu, Chem. Mater., 29 (2017) 10526-10533.

[29] N. Priyadharsini, S. Shanmugapriya, P.R. Kasturi, S. Surendran, R.K. Selvan, Electrochim. Acta, 289 (2018) 516-526.

[30] X. Rui, X. Zhao, Z. Lu, H. Tan, D. Sim, H.H. Hng, R. Yazami, T.M. Lim, Q. Yan, ACS Nano, 7 (2013) 5637-5646.

[31] C.F. Holder, R.E. Schaak, ACS Nano, 13 (2019) 7359-7365.

[32] Y. Wan, D. Zhao, Chem. Rev., 107 (2007) 2821-2860.

[33] S. Yu, A. Mertens, H. Kungl, R. Schierholz, HermannTempel, Rüdiger-A.Eichel, Electrochim. Acta, 232 (2017) 310-322.

[34] X. Wu, F. Rohman, M. Meledina, H. Tempel, R. Schierholz, H. Kungl, J. Mayer, R.-A. Eichel, Electrochim. Acta, 279 (2018) 108-117.

[35] N. Laszczynski, A. Birrozzi, K. Maranski, M. Copley, M.E. Schuster, S. Passerini, J. Mater. Chem. A, 4 (2016) 17121-17128.

[36] N.N. Bramnik, K. Nikolowski, C. Baehtz, K.G. Bramnik, H. Ehrenberg, Chem. Mater., 19 (2007) 908-915.

[37] F.C. Strobridge, R.J. Clement, M. Leskes, D.S. Middlemiss, O.J. Borkiewicz, K.M. Wiaderek, K.W. Chapman, P.J. Chupas, C.P. Grey, Chem. Mater., 26 (2014) 6193-6205.

[38] K.J. Kreder, A. Manthiram, ACS Energy Lett., 2 (2016) 64-69.

[39] H. Wang, Y. Yang, Y. Liang, L.F. Cui, H. Sanchez Casalongue, Y. Li, G. Hong, Y. Cui, H. Dai, Angew. Chem., 123 (2011) 7502-7506.

[40] Y. Maeyoshi, S. Miyamoto, Y. Noda, H. Munakata, K. Kanamura, J. Power Sources, 337 (2017) 92-99.

[41] J. Ludwig, C. Marino, D. Haering, C. Stinner, D. Nordlund, M.M. Doeff, H.A. Gasteiger, T. Nilges, RSC Adv., 6 (2016) 82984-82994.

[42] F. Teng, M. Chen, G. Li, Y. Teng, T. Xu, S.-i. Mho, X. Hua, J. Power Sources, 202 (2012) 384-388.

[43] Y. Long, Y. Shu, X. Ma, M. Ye, Electrochim. Acta, 117 (2014) 105-112.

[44] A.J. Bard, L.R. Faulkner, J. Leddy, C.G. Zoski, Electrochemical methods: fundamentals and applications, wiley New York, 1980.

[45] V. Ramar, P. Balaya, Phys. Chem. Chem. Phys., 15 (2013) 17240-17249.

[46] X. Wang, H. Hao, J. Liu, T. Huang, A. Yu, Electrochim. Acta, 56 (2011) 4065-4069.